

Simulation of Two- and Three-Dimensional Dense-Fluid Shear Flows *via* Nonequilibrium Molecular Dynamics. Comparison of Time-and-Space-Averaged Stresses from Homogeneous Doll's and Sllod Shear Algorithms with those from Boundary-Driven Shear.

Wm. G. Hoover and Carol G. Hoover

Ruby Valley Research Institute

Highway Contract 60, Box 598, Ruby Valley 89833, NV USA

Janka Petravac

Complex Systems in Biology Group

Centre for Vascular Research

The University of New South Wales

Sydney NSW 2052, Australia

(Dated: November 6, 2018)

Abstract

Homogeneous shear flows (with constant strainrate dv_x/dy) are generated with the Doll's and Sllod algorithms and compared to corresponding *inhomogeneous* boundary-driven flows. We use one-, two-, and three-dimensional smooth-particle weight functions for computing instantaneous spatial averages. The nonlinear normal stress differences are small, but significant, in both two and three space dimensions. In homogeneous systems the sign and magnitude of the shear-plane stress difference, $P_{xx} - P_{yy}$, depend on both the thermostat type and the chosen shearflow algorithm. The Doll's and Sllod algorithms predict opposite signs for this normal stress difference, with the Sllod approach definitely wrong, but somewhat closer to the (boundary-driven) truth. *Neither* of the homogeneous shear algorithms predicts the correct ordering of the kinetic temperatures: $T_{xx} > T_{zz} > T_{yy}$.

PACS numbers: 02.70.Ns, 45.10.-b, 46.15.-x, 47.11.Mn, 83.10.Ff

Keywords: Thermostats, Ergostats, Molecular Dynamics, Computational Methods, Smooth Particles

I. INTRODUCTION

In the present work, we use nonequilibrium molecular dynamics[1] to study microscopic simulations of “simple shear flow” (also called “plane Couette flow”):

$$v_x \propto y \rightarrow P_{xy} \equiv P_{yx} \equiv -\eta[(\partial v_x/\partial y) + (\partial v_y/\partial x)] = -\eta(dv_x/dy) = -\eta\dot{\epsilon} .$$

The flow is in the x direction so that the tensor ∇v has only one nonzero element, $(\nabla v)_{yx} = dv_x/dy = \dot{\epsilon}$. We use the symbol P for the (symmetric second-rank Cauchy) pressure tensor (positive in compression and the negative of the stress tensor, $P = -\sigma$); v for the (time- and space-dependent) hydrodynamic flow velocity; η for the shear viscosity; and $\dot{\epsilon}$ for the magnitude of the imposed (or measured) shear strain rate. The various simulation types we consider here were designed to clarify the relationships between periodic homogeneous methods, thermostated *everywhere*, and flows with moving thermostated *boundaries*. All the methods we use are consistent with Green and Kubo’s linear response theory at small rates of shear[2]. We are specially interested in characterizing and understanding the *nonlinear* shearplane stress difference: $[P_{xx} - P_{yy} = \sigma_{yy} - \sigma_{xx}]$ which arises in sufficiently small systems at sufficiently large shear rates. In carrying out microscopic simulations both the boundary conditions and the thermostats or ergostats which control the flow need to be carefully considered[1].

Though simple shear flow is “stationary”, *fluctuations* in local properties necessitate *averaging*, both in time and in space. Here we reduce the importance of these fluctuations by using spatial averaging techniques borrowed from smooth-particle continuum simulation methods[3]. We measure instantaneous *spatially-averaged* flow velocity, temperature, and pressure-tensor components.

The two best-known homogeneous microscopic methods, the Doll’s tensor[4] and Sllod algorithms[5], treat fluid rotation differently, leading to qualitatively different predictions for the nonlinear normal stress difference. *Boundary-driven* flows can help to resolve this disagreement[6, 7, 8, 9]. *Useful* flows need to satisfy four conditions: the spatial scale L of these flows needs to be large enough (relative to the particle size), but not too large (to avoid turbulence), with flow velocities v large enough (to emerge above fluctuations), but not too large (again, to avoid turbulence), in order to provide useful information. The relatively greater importance of fluctuations in two dimensions is responsible for the reduced utility of viscosity there, as shown in Fig. 1. Additionally, the frictional

boundary-fluid interaction needs to be sufficiently strong to prevent excessive boundary slip.

In the present work, we carry out both two- and three-dimensional simulations using all three approaches (Doll's, Sllod, and boundary-driven) for two simple, and rather similar, pairwise-additive repulsive potentials. We focus here on the normal stress difference, $P_{xx} - P_{yy} = \sigma_{yy} - \sigma_{xx}$, in the shearplane. We will see that the Doll's and Sllod algorithms typically predict different signs for the simple monatomic dense fluids considered here. Both these *homogeneous* algorithms yield clearcut results, insensitive to system size.

In the early days of such shearflow simulations[10] it was thought that the two-dimensional viscosity might depend logarithmically on system size[11]. More recently, careful studies[12, 13, 14, 15] of the corresponding Green-Kubo stress-stress correlation function:

$$\eta = (V/kT) \int_0^\infty \langle P_{xy}(0)P_{xy}(t) \rangle_{\text{eq}} dt ,$$

indicate no such dependence in dense fluids. The work we carry out here is consistent with this lack of size dependence. Here we find that the coefficient of the hypothetical logarithmic viscosity contribution can be no larger than 10^{-4} in the natural reduced units of atomic size, mass, and velocity. The more realistic *boundary-driven* flows necessarily entail larger fluctuations and considerable size dependence. We are nevertheless able to determine the sign and the size of the normal stress difference for such flows so as to characterize the errors inherent in the homogeneous algorithms.

This paper is organized as follows: in Sec. II we lay out the macroscopic description of the problem; in Sec. III the *microscopic* description; In Sec. IV we describe the two homogeneous algorithms emphasizing their similarities and differences; in Sec. V we describe the boundary-driven algorithm used in the present work; Sec. VI describes the smooth-particle spatial averaging method used in analyzing results from simulations; Sec. VII describes numerical results for two similar (smooth repulsive) forcelaw models in two very-different density regimes and in two space dimensions; Sec. VIII describes corresponding three-dimensional results for one of these forcelaw models; Sec. IX lists the conclusions we have drawn from this work.

Figure 1

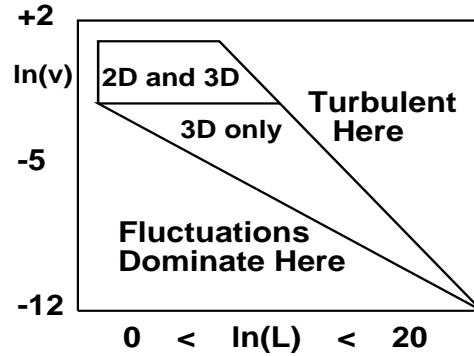


Figure 1: Limits imposed on system size L and boundary velocity v by atomistic size, thermal fluctuations, turbulence, and shockwaves. Viscosity is a useful concept for flows in the enclosed areas. The figure here is constructed for a fluid at unit mass, number density, temperature, viscosity, and heat conductivity. L is measured in units of the microscopic particle size and v is measured in units of the thermal velocity. Modeled after Ref. [6].

II. MACROSCOPIC DESCRIPTION OF SIMPLE SHEAR FLOW

Classical fluid flow can be modeled and understood from either the microscopic or the macroscopic standpoint. In the *microscopic* description individual particles obey the *ordinary* differential equations of motion of nonequilibrium molecular dynamics[1]:

$$\{ m\ddot{r} = m\dot{v} = F_A + F_B + F_C + F_D \} ,$$

and everything follows from the functional forms of the assumed atomistic, boundary, constraint, and driving forces[1, 16]. In molecular dynamics, just as in continuum hydrodynamics, the pressure tensor is (defined to be) the *comoving momentum flux*, comoving relative to the flow velocity. In a many-body system with forces derived from the pairwise-additive pair potential $\phi(r)$, the pressure tensor is made up of $\{i, j\}$ pair contributions as well as individual particle convective contributions[1]:

$$P_{xy}V = \sum_{i<j} \left(\left[\frac{xy}{r^2} \right] [F \cdot r] \right)_{ij} + \sum_i (p_x p_y / m)_i ;$$

$$x_{ij} \equiv x_i - x_j ; y_{ij} \equiv y_i - y_j ; r_{ij} \equiv |r_i - r_j| ; F_{ij} \equiv -\nabla_i \phi(r_{ij}) .$$

It is evident that the pair-potential pressure tensor is *symmetric*, with P_{xy} and P_{yx} equal.

In the *macroscopic* description the continuum field variables [such as the mass density $\rho(r, t)$, the velocity $v(r, t)$, and the energy per unit mass $e(r, t)$] obey *partial* differential

equations:

$$\begin{aligned}\dot{\rho} &= -\rho \nabla \cdot v ; \\ \rho \ddot{r} &= \rho \dot{v} = -\nabla \cdot P = \nabla \cdot \sigma ; \\ \rho \dot{e} &= -\nabla v : P - \nabla \cdot Q .\end{aligned}$$

In these general continuum field equations the *constitutive relations* for the stress tensor $\sigma \equiv -P$ and the heat flux vector Q distinguish one material from another. In both approaches a computational algorithm for solving the equations is needed. Its implementation gives $\{ r(t), v(t) \}$ in the microscopic case and $\{ \rho(r, t), v(r, t), e(r, t) \}$ in the macroscopic case). In either case, a well-posed problem also requires boundary and initial conditions, constraints, and driving forces.

First consider the simplest model system illustrating stationary simple shear: imagine an incompressible Newtonian fluid, with constant shear viscosity η , and which also follows Fourier's linear heat transport law with a constant heat conductivity κ :

$$\begin{aligned}P_{xy} &= -\eta [(dv_x/dy) + (dv_y/dx)] ; \\ \rho \dot{e} &= \kappa \nabla^2 T - P : \nabla v .\end{aligned}$$

We ignore thermal expansion, so that the mass density ρ is constant. We denote the local thermodynamic variables in the conventional way: temperature $T(r)$, pressure tensor $P(r)$, and internal energy per unit mass $e(r)$. We adopt the colon convention in the tensor product $A : B$ to indicate a sum over all four $A_{ij}B_{ij}$ terms in two dimensions, and all nine such terms in three dimensions. In some texts the alternative sum (immaterial for the symmetric tensors considered here) $A_{ij}B_{ji}$ is used.

Simple shear flow for this bare bones textbook model is perhaps the simplest imaginable nonequilibrium flow problem. It gives a *linear* variation of velocity in space along with a *quadratic* variation of temperature. Simple shear flow can be driven by two moving parallel boundaries, both of them at temperature T_B , and able to absorb heat and to impose their boundary velocities, $v_x = \pm v$, on a two-dimensional strip or three-dimensional slab of model fluid of thickness L :

$$v_x(y = \pm L/2) = \dot{\epsilon} y .$$

The stationary macroscopic description of such a flow, for the model Newtonian fluid with Fourier heat conduction, has a constant stress tensor, a *linear* velocity profile and

Figure 2

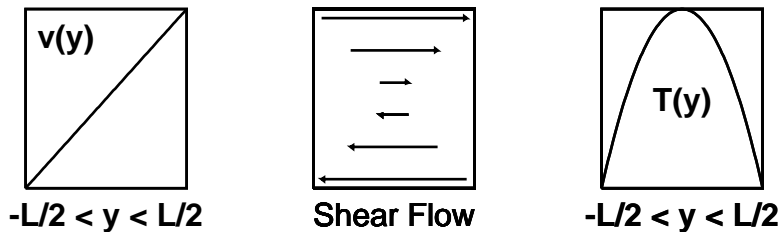


Figure 2: The simple shear flow indicated in the center panel corresponds to the linear velocity profile (shown to the left) and quadratic temperature profile (shown at the right). The nonlinear effects considered in this paper give relatively small deviations from these idealized profiles.

(because $\nabla^2 T$ is constant) a *quadratic* temperature profile:

$$(dv_x/dy) = \dot{\epsilon} = 2v/L = -P_{xy}/\eta ;$$

$$\Delta T(y) = T(y) - T_B = (\eta \dot{\epsilon}^2 / 2\kappa)[(L/2) - y][(L/2) + y] .$$

The maximum temperature difference, relative to the boundaries' temperature T_B ,

$$\Delta T(y) \leq \Delta T_{\max} = \Delta T(0) = \eta \dot{\epsilon}^2 L^2 / 8\kappa = \eta v^2 / 2\kappa ,$$

occurs at the midplane $y = 0$. See Fig. 2 for a schematic illustration of this prototypical simple shear flow.

This stationary solution satisfies *energy balance*, with the rate at which heat is generated throughout the volume V (necessarily the same as the rate at which external work is done, $-\dot{W}$) equal to the rate at which heat is transferred through the two boundary walls of area (length in two dimensions) A , at $y = \pm L/2$:

$$-\dot{W} = -P_{xy}V\dot{\epsilon} = \eta V\dot{\epsilon}^2 = \kappa A[(dT/dy)_{-L/2} - (dT/dy)_{+L/2}] .$$

This macroscopic description of shear flow guides our interpretation of microscopic simulations. We focus on the complications caused by fluctuations and nonlinearities in what follows.

III. MICROSCOPIC DESCRIPTION OF SIMPLE SHEAR FLOW

Molecular dynamics was developed over 50 years ago [17, 18, 19] and soon gave rise to successful interpretations of equilibrium properties based on hard-sphere perturbation-

theory[20] analogous to Enskog’s hard-sphere understanding of dense-fluid transport properties[21]. Field-driven diffusion[22], shear and bulk viscous flows[23], and heat conducting flows[24, 25] all came to be simulated with a variety of algorithms. Special boundary conditions and computational thermostats were developed to model these flows. Throughout this development the limiting case of Green and Kubo’s linear theory of transport served as a guide[26].

In the past thirty years simulation has come a long way. *Billions* of atoms can be simulated now[27]. Nonequilibrium simple-shear algorithms have been developed for diatomic and polyatomic molecules[28, 29], not just simple fluids. More recently, alternative shear-flow algorithms have been developed for periodic irrotational “elongational” flows[30, 31, 32], flows with a steady stretching in one direction and a simultaneous shrinking in a perpendicular direction. It might be thought (as it once was[33]) that such a flow could not be followed forever, but a clever choice of periodic boundaries makes it possible to study steady thermostated elongational flows. The conceptual difficulties involved in deriving these algorithms have led to a spirited literature[34, 35, 36] as to the “correctness” of the various algorithms. Such discussions can easily lead outsiders to the impression that it is hard to distinguish “correct” from “incorrect” algorithms.

The controversial aspects of these shear-flow algorithms[28, 29, 30, 31, 32, 33, 34, 35, 36] led us to reconsider the problem. It seemed to us that a fresh look at the basic algorithms for monatomic simple-shear flows would help to develop a perspective clarifying this situation. It is evident that the nonlinear aspects of the computer algorithms are to some extent arbitrary, as the only true guidelines for correctness are consistency with the well-known and well-accepted *linear* flow theory described by Newtonian viscosity and Fourier heat conduction.

In *viscous* shear flow, which we consider here, *any* reasonable algorithm needs to satisfy the requirement that the shear viscosity for small strain rates agrees with Green and Kubo’s linear-response relation[2, 26] linking the viscosity to equilibrium fluctuations in the shear stress $\sigma_{xy} = -P_{xy}$:

$$\eta = (V/kT) \int_0^\infty \langle P_{xy}(0)P_{xy}(t) \rangle_{\text{eq}} dt ;$$

$$\eta = \frac{-P_{xy}}{\dot{\epsilon}} ; \dot{\epsilon} \equiv \frac{\partial v_x}{\partial y} + \frac{\partial v_y}{\partial x} .$$

For simplicity we consider systems with pairwise-additive forces $\{F_{ij}\}$ derived from a

potential function $\Phi = \sum \phi$:

$$\{ F_{ij} = -\nabla_i \phi(|r_i - r_j|) = -F_{ji} \} ,$$

In such a system both the energy E ,

$$E = \Phi + K = \sum_{i<j} \phi_{ij} + \sum_i p_i^2/2m ,$$

and the microscopic pressure tensor P ,

$$PV = \sum_{i<j} (Fr)_{ij} + \sum_i (pp/m)_i ,$$

are sums of two-particle potential and single-particle kinetic contributions.

There are two interesting ambiguities in the definition of pressure in a particulate system. The contributions of the potential pair interaction terms $\{ (Fr)_{ij} \}$ to PV need to be allocated spatially. Either delta-function contributions at r_i and r_j , or at $(r_i + r_j)/2$, or *smoothed* distributions centered at these locations can be used. The old ‘‘Irving-Kirkwood’’ preference for delta functions is motivated more by analytic convenience than by any physical considerations. A *smoothed* approach is certainly preferable in computational work.

The kinetic part of PV is ambiguous too. How is the ‘‘comoving’’ velocity to be defined in a system with transient velocity fluctuations? Either an instantaneous or a time-averaged hydrodynamic velocity can be chosen. Only the *kinetic* part of $P_{xy}V$ is affected by this choice. The simplest versions of the two choices are as follows:

$$P_{xy}^K(t)V \equiv \sum_i m[v_x^i - v_x(t)][v_y^i - v_y(t)] \text{ (instantaneous)}$$

or

$$P_{xy}^K(t)V \equiv \sum_i m[v_x^i - \langle v_x \rangle_{\text{time}}][v_y^i - \langle v_y \rangle_{\text{time}}] \text{ (time averaged)} .$$

The kinetic part of the pressure tensor is the usual definition of the instantaneous kinetic *temperature* for N particles[37]. In three space dimensions the usual definitions of $\{T_{xx}, T_{yy}, T_{zz}\}$ are:

$$NkT_{xx}(t) = \sum^N m(v_x^i - \langle v_x(t) \rangle)^2 ;$$

$$NkT_{yy}(t) = \sum^N m(v_y^i - \langle v_y(t) \rangle)^2 ;$$

$$NkT_{zz}(t) = \sum^N m(v_z^i - \langle v_z(t) \rangle)^2 ,$$

where the average velocity at time t is computed by summing N individual particle velocities.

The instantaneous hydrodynamic velocity $(v_x(t), v_y(t))$ has to be estimated numerically. The simplest way to do this in a system composed of moving particles, is to use a weighted (smoothed-particle) average of nearby particle velocities:

$$v(t) \equiv \sum_i v_i w_{ir} / \sum_i w_{ir} ; w_{ir} = w(|r - r_i|) ,$$

where the time-independent scalar weight function w_{ir} has a finite spatial range, and emphasizes the contributions of those nearby particles to the location r where $v(t)$ is to be computed. The details of this spatial average are described in Section VII. Fortunately, the main conclusions of this work are independent of the necessarily arbitrary choice between using instantaneous and time-averaged flow velocities. By choosing to study stationary simple shear we avoid the additional complexities associated with *time* averaging flows which have an explicit time dependence in their boundary conditions.

The atomistic simulation approach is also complicated by heat and by fluctuations. Because viscosity is *dissipative*, a viscous shear flow necessarily generates *heat*. Particle motions and collisions in systems tractable with molecular dynamics necessarily exhibit fluctuations in *all* their local properties[38]. Despite the time-reversibility of the underlying equations of motion, the overall longtime-averaged character of these flows *is* necessarily dissipative, in accord with macroscopic hydrodynamics and the Second Law of Thermodynamics[38, 39, 40, 41].

To simulate a *steady* viscous flow, the heat generated needs to be removed. This can be done with any one of many schemes, all of which are based on time-reversible constraint forces[1, 16]. Such constraint forces can play the rôle of a feedback-based thermostat or ergostat,

$$\{ F_{\text{Constraint}} = -\zeta p \} \rightarrow \dot{K} \equiv 0 \text{ or } \dot{E} \equiv 0 .$$

Typical constraint-force choices keep the kinetic energy K or the total energy E fixed, or allow these energies to fluctuate about a specified mean value in a way consistent with Gibbs' statistical mechanics at equilibrium[42, 43]. For simplicity, we restrict ourselves here to ‘‘Gaussian thermostats’’ [so named after Gauss' Principle of Least Constraint][44] which fix the kinetic energy K or the total energy E of a particular set of degrees

of freedom by imposing feedback-based constraint forces, $\{ F_{\text{Constraint}} = -\zeta p \}$. The Gaussian “friction coefficient” ζ constrains the momenta $\{ p \}$ contributing to K or E . We next describe the two best-known computational algorithms for simulating simple shear.

IV. DOLL’S AND SLLOD ALGORITHMS FOR SIMPLE SHEAR FLOW

Shear flows were the first application of *homogeneous* nonequilibrium molecular dynamics[6]. Steady *inhomogeneous* shockwaves[45] and boundary-driven shear flows[6, 7, 8, 9] had both been simulated earlier. Special boundary conditions, or external forces, as well as thermostats had to be developed for the homogeneous shear flows. The numerical applications of these ideas, in the early 1970s, preceded their formal theoretical development by decades. The Doll’s Tensor Hamiltonian for viscous flows was discovered in 1985[4]; Dettmann and Morriss’ Hamiltonians (for the Nosé-Hoover and Gauss thermostats) were discovered in 1996[46, 47]; and a proper formulation of elongational flows first appeared in 1998[30].

Simple homogeneous shear flow, with the x velocity proportional to the y coordinate,

$$\dot{\epsilon} \equiv dv_x/dy \longleftrightarrow \nabla v \equiv \begin{bmatrix} \frac{\partial v_x}{\partial x} & \frac{\partial v_y}{\partial x} \\ \frac{\partial v_x}{\partial y} & \frac{\partial v_y}{\partial y} \end{bmatrix} = \begin{bmatrix} 0 & 0 \\ \dot{\epsilon} & 0 \end{bmatrix},$$

can be implemented with periodic “Lees-Edwards” boundary conditions[48] [developed independently by Bill Ashurst in his Ph D thesis work][7]. See page 26 of Ref. [6] for a brief description of Ashurst’s algorithm. The corresponding flow is illustrated in Figure 3.

This simple shear flow, with $\frac{\partial v_x}{\partial y}$ nonzero, is “rotational”, in the sense that the clockwise rotation rate, $-\omega$, is nonzero, and equal to half the strain rate:

$$-\omega \equiv [(\partial v_x/\partial y) - (\partial v_y/\partial x)]/2 = \dot{\epsilon}/2 .$$

In our specific special case ∇v can be written as a sum of irrotational and rotational contributions:

$$\nabla v = \begin{bmatrix} 0 & 0 \\ \dot{\epsilon} & 0 \end{bmatrix} = \begin{bmatrix} 0 & +\dot{\epsilon}/2 \\ +\dot{\epsilon}/2 & 0 \end{bmatrix} + \begin{bmatrix} 0 & -\dot{\epsilon}/2 \\ +\dot{\epsilon}/2 & 0 \end{bmatrix} .$$

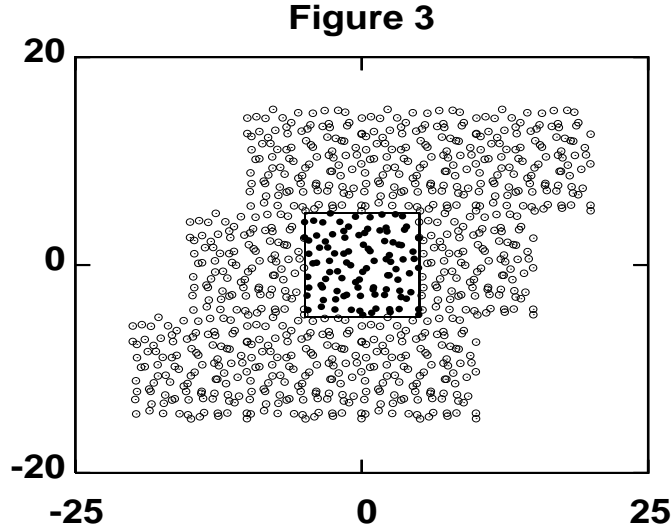


Figure 3: Periodic 100-particle shear flow, showing eight periodic $L \times L$ images of the central 10×10 box. The particle velocities in the images above/below the central N -particle box differ from those of the central box by $\pm \epsilon L$.

See Figure 3 for an illustration of the periodic boundary conditions consistent with such a flow. A stationary nonequilibrium state can result if the irreversible heating rate, $-\dot{W} = \eta \dot{\epsilon}^2 V$ is appropriately compensated by momentum-dependent thermostat forces.

The Doll’s and Sllod algorithms are straightforward possibilities for simulating such a flow, and the differences between them are small (of order $\dot{\epsilon}^2$) at moderate strain rates. Ashurst’s periodic shear algorithm preceded the formal derivations of differential evolution equations for the shear flow and its associated thermostats. His finite-difference algorithm was equivalent, for small timesteps, to a thermostated version of what is now called the Sllod algorithm:

$$\{ \dot{x} = (p_x/m) + \dot{\epsilon} y ; \dot{y} = (p_y/m) ; \dot{p}_x = F_x - \dot{\epsilon} p_y - \zeta p_x ; \dot{p}_y = F_y - \zeta p_y \} .$$

In the absence of the thermostat forces $\{ -\zeta p \}$, these motion equations give an energy change exactly consistent with the rate at which thermodynamic work is performed by the instantaneous shear stress $-P_{xy}$.

In the alternative Doll’s-Tensor approach[4], a coordinate-momentum (q, p) sum [giving rise to the “Kewpie-Doll” name] is added to the usual Hamiltonian. The added term

includes the strain rate $\dot{\epsilon}$:

$$\mathcal{H}_{\text{Doll}} = \mathcal{H}_{\text{Usual}} + \dot{\epsilon} \sum_i (yp_x)_i .$$

The resulting Hamiltonian equations of motion,

$$\left\{ \dot{q} \equiv +\frac{\partial \mathcal{H}}{\partial p} ; \dot{p} \equiv -\frac{\partial \mathcal{H}}{\partial q} \right\} ,$$

are only slightly different to the closely related ‘‘Sllod’’ equations. The Doll’s tensor motion equations are

$$\left\{ \dot{x} = (p_x/m) + \dot{\epsilon}y ; \dot{y} = (p_y/m) ; \dot{p}_x = F_x ; \dot{p}_y = F_y - \dot{\epsilon}p_x \right\} .$$

In the absence of heat-extracting thermostats, both approaches, Sllod and Doll’s, provide an energy change exactly consistent with thermodynamics:

$$\dot{\mathcal{H}}_{\text{Doll}}(q, p, \nabla v) = 0 \rightarrow \dot{\mathcal{H}}_{\text{Usual}}(q, p) = -(d/dt) \sum qp : \nabla v \equiv -\dot{\epsilon}P_{xy}V .$$

The extra momentum-dependent forces, $\{-\dot{\epsilon}p_y\}$ for Sllod and $\{-\dot{\epsilon}p_x\}$ for Doll’s, model rotation. In a rotational flow in the xy plane the rotation rate ω is given by

$$\omega \equiv \frac{1}{2} \left[\frac{\partial v_y}{\partial x} - \frac{\partial v_x}{\partial y} \right] ,$$

and *corotating* momenta would include rotational contributions:

$$\dot{p}_x = -\omega p_y ; \dot{p}_y = +\omega p_x .$$

The Coriolis accelerations corresponding to rotation are similar in form to the momentum-dependent forces included in the Doll’s and Sllod algorithms.

It should be noted that the ambiguity in treating the atomistic rotation associated with shear has a relatively well-known analog in continuum mechanics[49]. In the plastic flow of solids the total macroscopic strain, idealized as a sum of elastic and plastic contributions, can only be computed by time integration: $\int \dot{\epsilon} dt \rightarrow \epsilon$. Because stress depends on strain, calculations involving plastic flow require the simultaneous time integration of an equation for stress evolution, $\int \dot{\sigma} dt \rightarrow \sigma$. If the effect of rotation on the stress is included (imagining that the stress rotates as if it were embedded in a rigid body) the ‘‘Jaumann stresses’’ result. These laboratory-frame stresses satisfy the evolution equations:

$$\dot{\sigma}_{xx} = -2\omega\sigma_{xy} ; \dot{\sigma}_{yy} = +2\omega\sigma_{xy} ; \dot{\sigma}_{xy} = \omega[\sigma_{xx} - \sigma_{yy}] .$$

A more complicated boundary-driven shear flow can be driven by imposing appropriate boundary conditions, including external thermostats or ergostats, on a Newtonian region with the usual equations of motion:

$$\{ \dot{x} = (p_x/m) ; \dot{y} = (p_y/m) ; \dot{p}_x = F_x ; \dot{p}_y = F_y \} .$$

The details of our boundary-driven simulations are given in Sec. VI. In his thesis work in the early 1970s Ashurst[7] found consistent shear viscosities for both boundary-driven and homogeneous periodic shear flows. More recently Liem, Brown, and Clarke made an effort to characterize the very nonlinear effects we seek in the present work in shear flow. They compared homogeneous shear (presumably using the Sllod approach) with a very large scale boundary-driven flow[9]. Unfortunately the limitations inherent in using such large systems made the nonlinear effects too small to measure.

V. BOUNDARY-DRIVEN SHEAR FLOW

To avoid dealing with free surfaces we have chosen to simulate fully-periodic four-chamber systems of the type shown in Figure 4. Posch and Hoover used the same geometry in an investigation of heat flow[50]. In two dimensions the system is made up of four $L \times L$ cells, each with an area one-fourth the total, $L^2 = N/4$. To eliminate surface effects the system is periodic in both x and y , with two steadily-moving chambers thermostated at a fixed kinetic temperature. The motion is induced by using steadily moving tethers. The remaining particles obey Newton's motion equations. This four-chamber geometry has a statistical advantage. The two Newtonian regions provide independent estimates of the stress and temperature tensor profiles. The differences between the two Newtonian regions provides a useful indication of the estimates' reliability. See, for instance, the normal-stress profiles for the two regions shown in Figs. 8, 10, and 11.

Though we do not give the results here, we have also considered a *two*-chamber periodically shearing flow geometry, in both two and three space dimensions. In the two-chamber approach the moving tethers' x velocities are

$$\{ \pm 1\epsilon L , \pm 3\epsilon L ; \pm 5\epsilon L ; \dots \} ,$$

in the odd-numbered cells, where L is the cell width, while the motion in the even-numbered cells is purely Newtonian. Just as in the four-chamber case periodic shearing

Figure 4

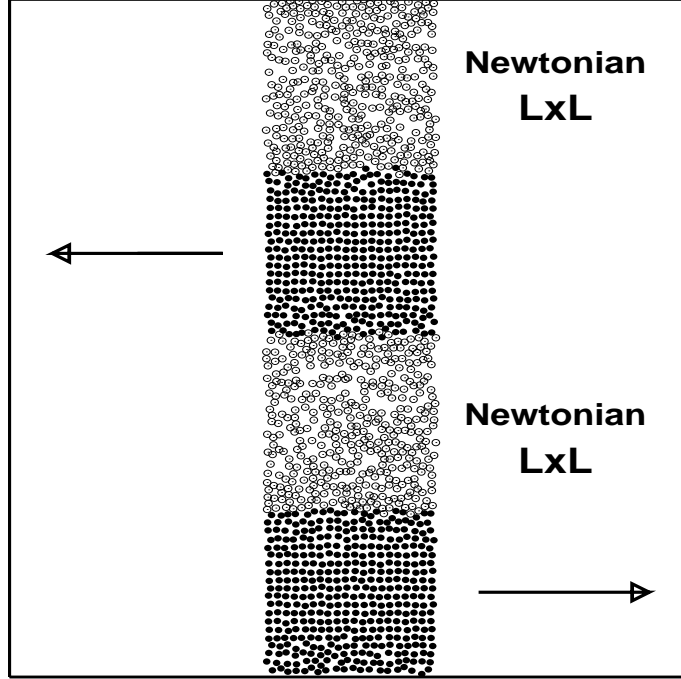


Figure 4: Four-chamber $L \times 4L$ periodic flow with 4×400 particles. Chamber 1 (filled circles at the bottom) moves to the right at speed $+\dot{\epsilon}L/2$; chamber 3 (filled circles, third chamber from the bottom) moves to the left at speed $-\dot{\epsilon}L/2$. This imposes the nominal strain rates $\mp\dot{\epsilon}$ on the two Newtonian chambers 2 and 4 (open circles). Periodic boundaries apply in both the x and the y directions. Note the ordering effect of the moving tethers in Chambers 1 and 3.

boundaries are used in all the space dimensions. The results from the two-chamber and four-chamber flows are not significantly different and are therefore not elaborated here.

The multi-chamber shear flows are induced by *tethering* the boundary particles to steadily moving lattice sites (a moving square lattice or simple cubic lattice, for convenience) with a simple quartic tethering potential, just as in the ϕ^4 model for heat conduction[51, 52]:

$$\phi^4 = \frac{\kappa_4}{4}[r - r_0(t)]^4 ; \dot{r}_0(t) = (\pm\dot{\epsilon}L/2, 0) .$$

Here the sites move. 100 is a good choice for the force constant κ_4 and gives better equilibration than tethers with alternative power-law exponents.

In order to prevent diffusive mixing between the Newtonian particles and the boundary particles it is useful to include a smooth repulsive boundary force returning errant Newtonian particles toward their chambers. For convenience this force has the same form as the boundary tethering forces used in the moving chambers. The fixed speed of the tethers, $|\dot{r}_0(t)|$, is chosen to impose overall strain rates $\pm\dot{\epsilon}$ on the two Newtonian regions. Whether or not the strain rate actually penetrates into the Newtonian regions depends upon whether or not “slip” occurs at the boundary, as we discuss in Sec. VIII B.

Because the heat generated by the shear varies as L^D in D dimensions, but must flow across a boundary of area (or length) L^{D-1} something “interesting” necessarily occurs as L increases. Eventually the driving chambers must become decoupled from the bulk Newtonian chambers so that both the work done and the corresponding heat generated actually decrease with increasing strain rate. In favorable cases, with good frictional coupling at the boundaries, this driving technique provides good velocity profiles and allows nonlinear effects to be determined. We turn next to the instantaneous smooth-particle spatial-averaging procedure required for analyzing the simulations.

VI. SMOOTH-PARTICLE SPATIAL AVERAGES

The spatial averaging algorithms our simulations require are borrowed from a continuum technique, “SPAM” [3]. Smooth particle applied mechanics (“SPAM”) is a technique for solving the partial differential continuum equations (continuity, motion, and energy) for the evolution of the density, velocity, and energy. It makes use of a normalized weight function with a maximum range h , $w(|r| < h)$. The weight function describes the spatial extent of a representative particle of mass m . The weight function is formulated with at least two continuous derivatives everywhere in order that the first and second continuum derivatives of smooth particle sums [corresponding to instantaneous local quantities such as $\nabla\rho(r, t)$, $\nabla v(r, t)$, and $\nabla^2 T(r, t)$], are everywhere continuous in both space and time. This continuity and differentiability facilitates a smooth transition between particle and continuum analyses.

Consider the two simplest cases, mass and momentum sums. The density $\rho(r)$, and the momentum density $\rho(r)v(r)$ at the location r are *defined* by summing up the contributions

of all particles $\{j\}$ within the maximum range h of that location:

$$\rho(r) \equiv m \sum_j w(|r - r_j|) = m \sum w_{rj} ;$$

$$\rho(r)v(r) \equiv m \sum_j v_j w(|r - r_j|) = m \sum w_{rj} v_j .$$

An advantage of this formulation is that the continuum continuity equation,

$$\frac{\partial \rho}{\partial t} = -\nabla \cdot (\rho v) ,$$

is satisfied *exactly* by the interpolated smooth particle fields:

$$\left(\frac{\partial \rho(r)}{\partial t} \right)_r = m \sum_j \left(\frac{\partial w(|r - r_j|)}{\partial t} \right)_r =$$

$$+m \sum_j (\nabla_j w_{rj}) \cdot \left(\frac{\partial |r - r_j|}{\partial t} \right)_r = +m \sum_j (\nabla_j w_{rj}) \cdot v_j =$$

$$-m \nabla_r \sum w_{rj} v_j \equiv -\nabla_r \cdot (\rho v) .$$

Notice that the spatial gradient operator, ∇_r , affects only $w(r - r_j)$ and not the individual point-particle properties $\{v_j\}$.

By choosing properly normalized weight functions spatial averages can be computed in one, two, or three spatial dimensions. The pressure tensor in the vicinity of a particle or at a grid point in three dimensions would be computed by using the *three*-dimensional weight function:

$$w_{3D}(r) = (105/16\pi h^3)[1 - 6(r/h)^2 + 8(r/h)^3 - 3(r/h)^4] \rightarrow \int_0^h 4\pi r^2 w_{3D}(r) dr \equiv 1 .$$

This particular weight function was discovered and used by Lucy in 1977[53]. It is the simplest normalized polynomial with (1) a maximum at $r = 0$; (2) a finite range $r < h$, and (3) two continuous derivatives vanishing at $r = h$. The corresponding one- and two-dimensional weight functions (for averages in thin strips or slabs, and for averages at particles or grid points in two-dimensional problems, are

$$w_{2D}(r) = (5/\pi h^2)[1 - 6(r/h)^2 + 8(r/h)^3 - 3(r/h)^4] \rightarrow \int_0^h 2\pi r w_{2D}(r) dr \equiv 1 .$$

$$w_{1D}(r) = (5/4h)[1 - 6(r/h)^2 + 8(r/h)^3 - 3(r/h)^4] \rightarrow \int_0^h 2w_{1D}(r) dr \equiv 1 .$$

The smooth-particle equations of motion for the time development of the individual particle velocities $\{v_j\}$ are generally formulated so as to conserve linear momentum exactly. The failure of this approach to conserve *angular* momentum is a relatively subtle point worthy of more research investigation[54].

VII. NUMERICAL RESULTS: TWO DIMENSIONS

A. Homogeneous Simulation Results with Lucy's Potential

To simplify the numerical work, reduce numerical integration errors, and to make contact with existing data[55, 56, 57], we initially chose to use Lucy's pair potential in two space dimensions. This pairwise-additive potential is identical to the weight function $w_{2D}(r)$ of the previous Sec. VI:

$$\phi(r) = \frac{5}{\pi h^2} [1 - 6x^2 + 8x^3 - 3x^4] ; x \equiv \frac{r}{h} < 1.$$

We can make a rough estimate of the potential contribution to the energy and pressure for this potential by assuming a *random* distribution of particles. Viewed as a statistical-mechanical potential function for molecular dynamics in two dimensions, Lucy's potential (due to the normalization of the Lucy weight function) then corresponds to the simple equation of state for a two-dimensional ideal gas:

$$\Phi = \sum_{i < j} \phi_{ij} = \frac{N^2}{2V} \leftrightarrow P^\Phi V = \frac{N^2}{2V} .$$

The energy expression follows from the normalization condition, while the pressure expression follows from the virial theorem:

$$P^\Phi V = \frac{1}{2} \sum r_{ij} \cdot F_{ij} \simeq -\frac{N^2}{4V} \int_0^h 2\pi r^2 \phi'(r) dr = \frac{N^2}{2V} .$$

At unit mass and number density and at a strain rate of $\dot{\epsilon} = 0.05$ the shear viscosity and normal stresses (for Sllod) were measured precisely in 1995[55, 56]. Because the results are insensitive to the number of particles used we list in Table I below only a single representative set of simulations for $N = 400$. The insensitivity of the viscosity to the algorithm type is also evident in Davis recent work[58].

We chose $h = 3$, for which the Sllod algorithm shear viscosity (with a single thermostat variable) has previously been computed. At unit density, with $L \times L = N$, the average number of pair interactions is approximately $14N$. We also used exactly the *same* Lucy's function as a *weight function*[3] for carrying out spatial averages. Table I lists the pressure-tensor components using both the Doll's and Sllod algorithms. The first four simulations are "isothermal" with both the average temperature, $(T_{xx} + T_{yy})/2$ thermostated (S1 and D1), and with both temperatures separately thermostated (S2 and D2), by using two

control variables, ζ_x and ζ_y . The last two simulations (SE and DE) constrain the internal energy rather than the temperature. Notice that in all these simulations the average pressure is fairly close to the simple virial-theorem estimate, $P^\Phi V/N \simeq 0.5$.

The normal stress difference is sensitive to the single-thermostat type:

$$P_{xx} - P_{yy} = +0.015 \text{ (Sllod)} ; P_{xx} - P_{yy} = -0.017 \text{ (Doll's)} ,$$

and is almost entirely kinetic. At the high effective density of these simulations the potential portion of the stress distribution is nearly isotropic. These results are essentially unchanged if energy, rather than average temperature, is controlled. On the other hand, this striking normal-stress effect disappears completely (because it is kinetic in nature) if the two temperatures are *separately* thermostated. We conclude from these simulations that a definitive determination of the normal stress difference requires a more realistic boundary-driven flow. One can have no confidence in nonlinear kinetic effects when the evolving kinetic energy itself can be dominated by the choice of homogeneous thermostats, one or two.

Table I. Relatively *high-density* Lucy viscosity in two dimensions. The mass and number densities are unity: $\rho = mN/V = N/V = 1$. The *range* of the Lucy potential is $h = 3$, so that each particle interacts simultaneously with approximately 30 neighbors. Space-and-time-averaged pressure tensors are given here for homogeneous Sllod and Doll's algorithms with a square periodic $20 \times 20 = 400$ -particle cell with a strain rate of $\dot{\epsilon} = dv_x/dy = 0.05$. The kinetic temperature is fixed, $kT = 0.07$, using a single control variable ζ (in the two runs S1 and D1) and two separate control variables in the x and y directions, ζ_x and ζ_y (in the two runs S2 and D2). The total energy is fixed at 0.500 for the runs SE and DE. The pressure-tensor components are given in the order xx, yy, xy with the kinetic, potential, and total terms indicated. The boundary conditions are periodic, with a total run time of $200 \times 10,000$ timesteps. The fourth-order Runge-Kutta timestep is 0.005. The average potential energies per particle for the first four runs are all in the range $0.4272 < \Phi/N < 0.4274$ so that the total energy in these runs is 0.497.

Figure 5

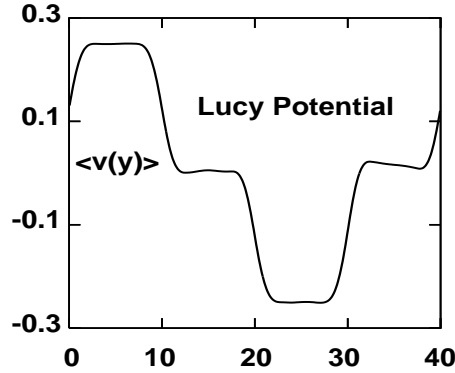


Figure 5: 400-particle Lucy velocity profile. See Fig. 4 for a 1600-particle analog. The two moving chambers correspond to the maximum and the minimum velocities. Here the two Newtonian chambers are so poorly coupled to the moving chambers that their mean velocities are nearly zero.

Run Type	P_{xx}^K	P_{xx}^Φ	P_{xx}^Σ	P_{yy}^K	P_{yy}^Φ	P_{yy}^Σ	P_{xy}^K	P_{xy}^Φ	P_{xy}^Σ
400S1	0.078	0.484	0.562	0.062	0.485	0.547	-0.022	+0.002	-0.021
400D1	0.060	0.486	0.546	0.079	0.483	0.563	-0.021	+0.001	-0.020
400S2	0.070	0.485	0.555	0.070	0.484	0.554	-0.025	+0.002	-0.023
400D2	0.070	0.485	0.555	0.070	0.484	0.554	-0.025	+0.002	-0.023
400SE	0.081	0.484	0.564	0.064	0.485	0.549	-0.023	+0.002	-0.022
400DE	0.062	0.486	0.548	0.083	0.483	0.566	-0.022	+0.001	-0.021

B. Boundary-Driven Simulation Results with Lucy’s Potential

Because the homogeneous investigations with the Lucy potential were sensitive to thermostat type, we next carried out several four-chamber simulations with two boundary chambers moving oppositely, as shown in Fig. 4. The density and strain rate were chosen to match the data in Table I. These simulations produced no useful normal-stress results! This failure reflects the nearly negligible coupling between the two moving chambers and the two Newtonian chambers. See the typical velocity profile in Fig. 5. Particles in the two Newtonian chambers simply rest quietly between the two rapidly moving walls. Evidently this very dense repulsive fluid with relatively weak collisional forces has insufficient friction for boundary driving to reach strain rates with significant nonlinear

Figure 6

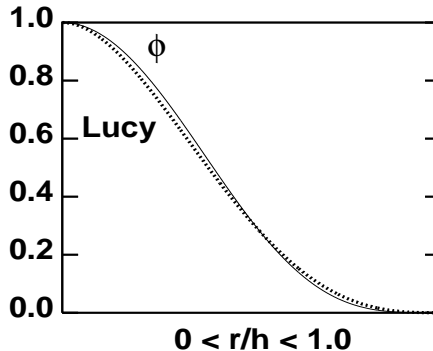


Figure 6: Comparison of Lucy’s potential and the short-ranged soft-sphere repulsive potential ϕ . The ordinate and the abscissa are divided by their maximum values, so that both scales vary from 0 to 1.

stress differences. This same difficulty was found by Liem, Brown, and Clarke in their three-dimensional Lennard-Jones simulations[9].

On the other hand, in Ashurst’s thesis work his “fluid-wall” boundary driving regions (velocity constraints, but no tethers, were used) produced good linear velocity profiles for both Lennard-Jones and soft-sphere potentials[6, 7]. Because those simulations correspond to a much lower density (with about three interactions per Lucy particle rather than thirty) and much more violent collisions than those of Table I we abandoned the high-density Lucy simulations and took up instead soft-disk and soft-sphere simulations at conditions more closely resembling those of Ashurst. The force law change was motivated by the desire to check our results with those from previous simulations[57]. The new simulations are discussed in the following two subsections.

C. Homogeneous Simulation Results with a Soft Disk Potential

Here we consider the short-ranged smooth soft-disk repulsive potential[57],

$$\phi(r < 1) = 100(1 - r^2)^4 ; r^2 = x^2 + y^2 ,$$

very similar in general shape to Lucy’s, but with *three* vanishing derivatives rather than just two, at its maximum range of unity. The two potentials are compared in Fig. 6. In comparison simulations we found that the two potentials provide quite similar normal stresses at corresponding temperatures and densities. Here we choose unit density and

energy per particle. We will see that boundary-driven simulations with this potential choice provide good velocity profiles, as did Ashurst’s similar “fluid walls” in 1972, and also allow comparisons with previous viscosity simulations in the same thermodynamic state. First we consider again Sllod and Doll’s simulations with homogeneous shear.

Just as in the Lucy simulations, the soft-disk normal stresses are quite different for the Doll’s and Sllod algorithms and are even less sensitive to system size. Now the short-ranged potential contribution to shear stress is actually dominant. The results listed in Table II, all using a single friction coefficient, fixing the energy per particle, $E/N = 1$, show that now the potential contribution to the stress difference is the same order as the kinetic contribution. The Sllod pressure difference is considerably smaller in magnitude:

$$P_{xx} - P_{yy} = +0.008 \text{ (Sllod)} ; P_{xx} - P_{yy} = -0.054 \text{ (Doll's)} ,$$

Because the rotated normal stress difference is equivalent to a shear stress:

$$\frac{(P_{xx} - P_{yy})}{2} \xleftrightarrow{45^\circ} P_{xy} ,$$

an alternative phenomenological description of the normal-stress effect corresponds to a rotation of the principal stress direction (the direction of maximum tension in the traceless stress tensor). The Doll’s algorithm gives a clockwise shear-stress rotation while the Sllod rotation is counterclockwise.

Table II. Moderate-density soft-disk viscosities. The range of the potential is unity so that each particle interacts, on the average, with only three neighbors at unit density. Space-and-time-averaged pressure tensors for homogeneous Sllod and Doll’s algorithms using the soft-disk pair potential illustrated in Fig. 6, $\phi = 100(1 - r^2)^4$. The energy and density are fixed, and equal to unity, and the strain rate, $\dot{\epsilon} = dv_x/dy$ is 0.50. The pressure-tensor components, are again given in the order xx, yy, xy with the kinetic, potential, and total terms indicated. The boundary conditions are periodic, with a total run time of 200x10,000 timesteps for $N = 64, 256, \text{ and } 1024$; 200x2000 timesteps for $N = 4096$, and 200x500 timesteps for $N = 16,384$. The fourth-order Runge-Kutta timestep is 0.005 and a single isoenergetic friction coefficient is used, as explained in Sec. II of the text.

N Type	P_{xx}^K	P_{xx}^Φ	P_{xx}^Σ	P_{yy}^K	P_{yy}^Φ	P_{yy}^Σ	P_{xy}^K	P_{xy}^Φ	P_{xy}^Σ
64S	0.690	3.217	3.907	0.681	3.223	3.904	-0.081	-0.534	-0.615
64D	0.679	3.201	3.880	0.692	3.240	3.932	-0.081	-0.535	-0.617
256S	0.691	3.214	3.904	0.682	3.216	3.898	-0.084	-0.538	-0.622
256D	0.679	3.195	3.873	0.694	3.235	3.929	-0.085	-0.538	-0.623
1024S	0.691	3.212	3.904	0.681	3.215	3.896	-0.085	-0.538	-0.623
1024D	0.679	3.193	3.872	0.694	3.235	3.928	-0.085	-0.537	-0.622
4096S	0.692	3.211	3.902	0.681	3.214	3.895	-0.085	-0.537	-0.623
4096D	0.679	3.193	3.872	0.693	3.235	3.928	-0.085	-0.538	-0.623
16384S	0.692	3.211	3.903	0.681	3.214	3.895	-0.085	-0.537	-0.623
16384D	0.679	3.193	3.872	0.694	3.233	3.926	-0.085	-0.537	-0.622

The Sllod program used to generate the data in Table II reproduced earlier Sllod results[57] for strain rates of 0.10 and 0.25 very well. Gass' Enskog-theory prediction[59] of the (linear) viscosity for the conditions of Table II, $\eta_{\text{Enskog}} = 1.5$, is just slightly higher than the value $\eta = 1.25$ given by the data in this Table. Just as in the work of Refs. [10]-[12] there is no indication of any logarithmic N -dependence in these results. Let us now compare these homogeneous results to those from boundary-driven simulations.

D. Boundary-Driven Results with the Soft-Disk Potential

With the soft-disk potential $\phi(r < 1) = 100(1 - r^2)^4$ a useful boundary-driven flow *does* result if the strain rate is moderate and the system is not too large. The boundary-driven flows *are* sensitive to system size. This is because the heat generated in a shear flow, of order L^D for L large eventually overwhelms the capacity of the boundary, of order L^{D-1} , to absorb it. The maximum strain rate that can be reached by boundary-driven flows is therefore limited by the heat conductivity as well as the efficiency of the frictional thermal contact at the reservoir walls. In addition to varying the size and stiffness of the tethering potential, we also varied the lattice structure of the tether sites, but settled on the simple square and cubic lattices when the pressure-tensor results proved to be insensitive to lattice type.

Systems with Newtonian strips 20 atoms wide were already large enough that no systematic deviation from linear stress behavior (with vanishing normal stress difference,

$\sigma_{xx} = \sigma_{yy} \simeq 0$), resulted. Accordingly we use a narrower system width here, 10, for an analysis of boundary driven flows. The system size is $N = 4 \times (10 \times 10) = 400$ particles.

Time-averaged boundary-driven velocity and normal-stress profiles are shown in the figures. The time-reversible frictional forces within the two steadily-moving “boundary” chambers were chosen to maintain a kinetic temperature in those chambers (relative to the tether velocity) of 0.70. This approximately reproduces the conditions of the Sllod and Doll’s states in Table II. Fig. 7 shows the average velocity $\langle v_x(y) \rangle$, computed using the one-dimensional weight function of Sec. VII. For each of 400 equally-spaced gridpoints the instantaneous values of the laboratory-frame velocity components $\{\dot{x}_i\}$ were spatially averaged at the grid points:

$$v_x(y_G, t) \equiv \sum_i \dot{x}_i w_{1D}(|y_G - y_i(t)|) / \sum_i w_{1D}(|y_G - y_i(t)|)$$

These instantaneous gridpoint averages were then themselves averaged over time and are plotted in Fig. 7.

Pressure-tensor components at each particle were calculated in two different ways. Using the *assumed analytic form, a linear velocity profile*,

$$\begin{aligned} 0 < y < 10 &\longrightarrow \langle v_x \rangle_{\text{analytic}} = +5 ; \\ 10 < y < 20 &\longrightarrow \langle v_x \rangle_{\text{analytic}} = 15 - y ; \\ 20 < y < 30 &\longrightarrow \langle v_x \rangle_{\text{analytic}} = -5 ; \\ 30 < y < 40 &\longrightarrow \langle v_x \rangle_{\text{analytic}} = y - 35 , \end{aligned}$$

the pressure tensors for particles in the vicinity of each grid point were computed as averages, using the two-dimensional weight function $w_{2D}(r < h = 3)$. These individual pressure-tensor components were then averaged, with $w_{1D}(r < h = 3)$ as were the velocities of Fig. 7. Pressure-tensor components were also computed and averaged using the smooth-particle weights $w_{2D}(r < 3)$ to calculate the *instantaneous* flow velocity $\langle v(r_j) \rangle$ at each particle j rather than using the assumed linear profile. The differences are relatively small, as can be seen in Fig. 8, where the two approaches are compared. Using the instantaneous velocity at each particle is analogous to, but smoother than, the “unbiased” procedure discussed by Evans and Morriss[16].

The normal stress differences following either approach are considerably larger than the Sllod results (Table II), and have the opposite sign to the Doll’s homogeneous results

Figure 7

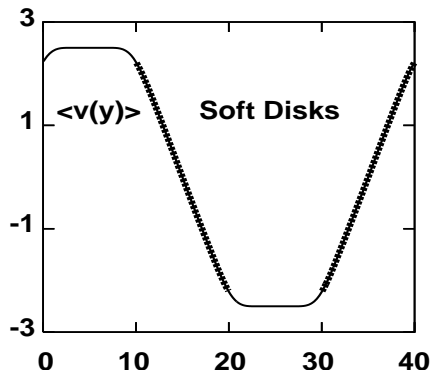


Figure 7: Velocity profile for a 400-particle system with the aspect ratio illustrated in Fig. 4. The tethering potential’s force constant, $\kappa = 100$ provides an efficient coupling between the *driving* chambers at $0 < y < 10$ and $20 < y < 30$ and the driven *Newtonian* chambers at $10 < y < 20$ and $30 < y < 40$. The locations of the two Newtonian chambers are emphasized in the velocity plot. The averaged velocity profile was calculated with the smooth-particle weighting function $w_{1D}(r < 3)$. The measured strain rate in the Newtonian regions is about ± 0.48 .

(Table II).

$$\frac{P_{xx} - P_{yy}}{2} \simeq 0.03 \text{ (Boundary-Driven) .}$$

The Sllod algorithm predicts a smaller effect (smaller by an order of magnitude) while the Doll’s algorithm predicts the wrong sign! We conclude that the two homogeneous algorithms provide no more than an order of magnitude estimate of the normal stress effects and further that these effects can be otherwise measured reliably, but with some difficulty.

Fig. 8 shows stresses for the two portions of the four-chamber system with $13 < y < 17$ and $33 < y < 37$. These portions have “typical” bulk fluid averages, without any influence from the two driving boundary regions. This is a consequence of the smooth-particle weight functions’ range, $h = 3$.

Figure 8

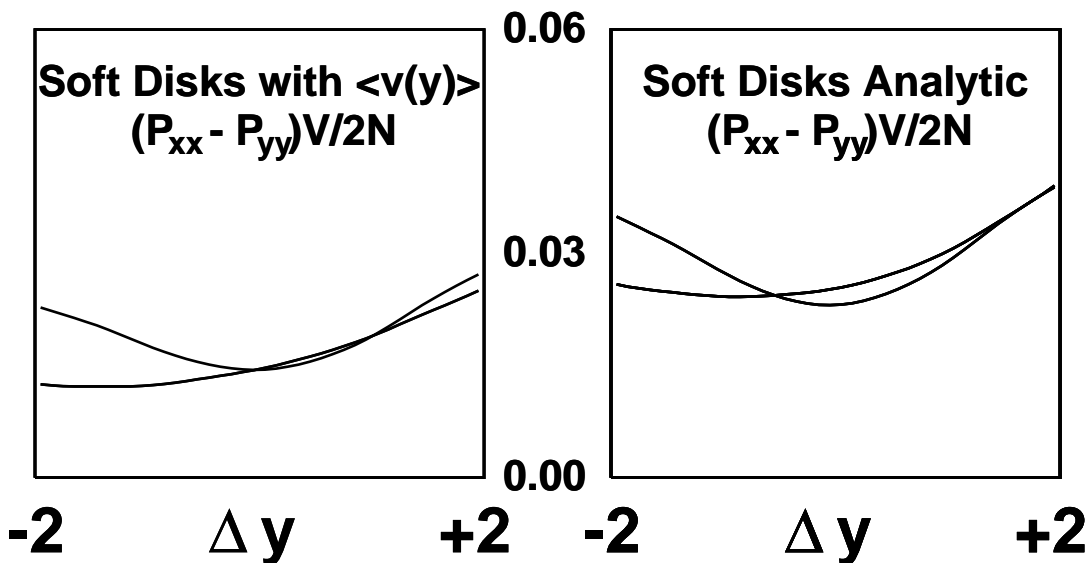


Figure 8: Boundary-driven two-dimensional flow using the “soft-disk” potential. Average normal stress differences are shown. At the left the stresses are calculated relative to the instantaneous velocity profile. There the spatially-averaged instantaneous velocity and stress at each particle are computed with w_{2D} , then averaged to get instantaneous profiles using w_{1D} , and finally time averaged. At the right the stresses are calculated relative to an assumed linear velocity profile. In both cases the stress difference is shown for the two regions $13 < y < 17$ and $33 < y < 37$ free of boundary influences and hence typical of bulk fluid. The run length was 5000.

VIII. NUMERICAL RESULTS: THREE DIMENSIONS

A. Periodic Shear

Three-dimensional boundary-driven simulations require only the addition of z coordinates, with periodic boundary conditions in the z direction. For comparison purposes, we first generated series of isoenergetic Sllod and Doll’s periodic shears. These results, shown in Table III, are for periodic shearing of $L \times L \times L$ cubes of soft-*sphere* fluid at unit density and energy:

$$\phi = 100(1 - r^2)^4 ; r^2 = x^2 + y^2 + z^2 ; N/V = Nm/V = E = K + \Phi \equiv 1 .$$

The constant-energy ergostat forces keep the total energy of the $N = L \times L \times L$ particles fixed. The kinetic energy K is a sum in which each particle’s contribution is measured

Figure 9

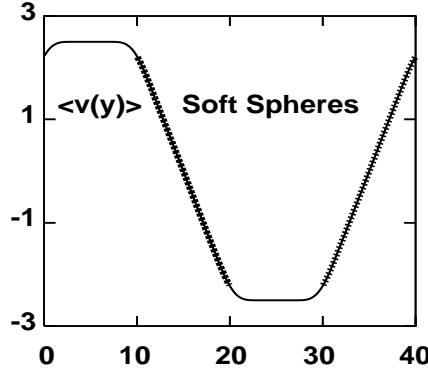


Figure 9: Time-averaged velocity profile for a 4000-particle three-dimensional system with the aspect ratio illustrated in Fig. 4. The tethering potential’s force constant, $\kappa = 100$ provides an efficient coupling between the *driving* chambers at $0 < y < 10$ and $20 < y < 30$ and the driven *Newtonian* chambers at $10 < y < 20$ and $30 < y < 40$. The locations of the two Newtonian chambers are emphasized in the velocity plot. The averaged velocity profile was calculated with the smooth-particle weighting function $w_{1D}(r < 3)$. The measured strain rate in the Newtonian regions is about ± 0.47 . The run length was 1000.

relative to the local velocity. Choosing the cube center as the coordinate origin, the systematic velocity in the x direction is taken to be proportional to y :

$$\{ p^2/2m \equiv [p_x^2 + p_y^2 + p_z^2]/2m ; (p_x/m) \equiv v_x - \dot{\epsilon}y \} .$$

The pressure-tensor results, given in Table III, are very insensitive to system size. Notice that the average kinetic temperature for all these isoenergetic simulations is approximately 0.5. The Sllod algorithm gives

$$T_{xx} > T_{yy} > T_{zz} \text{ (Sllod) ,}$$

while the Doll’s-Tensor algorithm gives instead

$$T_{yy} > T_{xx} > T_{zz} \text{ (Doll’s) .}$$

The (correct) “Boundary-Driven” results, described next, show instead the ordering

$$T_{xx} > T_{zz} > T_{yy} \text{ (Boundary - Driven) .}$$

The boundary-driven results also show qualitative differences from the Sllod and Doll’s results in the normal-stress differences, $(P_{xx} - P_{yy})$ and $(P_{xx} - P_{zz})$.

B. Boundary-Driven Shear

We next implemented $4000 = 4 \times (10 \times 10 \times 10)$ -particle boundary-driven shear flows similar to the two-dimensional flows of Sec. VIIB, but with periodic boundaries in the z direction and with a fixed isothermal boundary temperature 0.5, chosen to match the homogeneous periodic results. For comparison with these Sllod and Doll's results the same nominal strain rate, $dv_x/dy \simeq 0.5$ was used. Thus the two thermostated chambers move with velocities ($v_x = \pm 2.5$).

The time-and-spatially-averaged velocity profile computed with the weight function $w_{1D}(|\delta y| < 3)$ is shown in Figure 9. The measured strain rates in the straight-line portions of the profile are about ± 0.47 . The energy dissipation rate for 6000 thermostated degrees of freedom in the two moving 1000-particle reservoirs was $6000kT\langle\zeta\rangle = 6000 \times 0.5 \times 0.112 = 336$, giving an estimate for the viscosity:

$$\eta = T\dot{S}_{\text{external}}/(V\dot{\epsilon}^2) = 336/(2000 \times 0.5^2) = 0.672 ,$$

within two percent of the periodic result, 0.688 from Table III. The Newtonian shear stresses from the $4000 = 4 \times (10 \times 10 \times 10)$ -particle simulation are ± 0.37 in the bulk Newtonian regions, corresponding to

$$\eta = -P_{xy}/(dv_x/dy) = 0.74 .$$

The time-averaged spatially-smoothed normal stress differences,

$$(P_{xx} - P_{yy})/2 \simeq 0.01 ; (P_{xx} - P_{zz})/2 \simeq 0.01 ,$$

are only different with marginal significance, and are shown in Figs. 10 and 11. We considered three different system sizes, to ensure that these results are insensitive to small geometrical changes. Data for $N = 4 \times 10^3$ (run length 1000), $N = 4 \times 12^3$ (two runs of length 500; results from only one of them are shown here as the difference between the two was insignificant), and $N = 4 \times 14^3$ (run length 400) are included in the figures. Just as before, the Newtonian regions for which the data are plotted are those free of any boundary influences in the stress averaging. The corresponding Sllod and Doll's values for the stress differences, +0.003 and -0.016, respectively, are quite different, just as in two dimensions. The disparity shows that neither homogeneous algorithm is even close to "correct". The actual difference between P_{yy} and P_{zz} is apparently quite small, while

both the Doll's and the Sllod algorithms indicate a relatively large difference of order ± 0.04 . The statistical fluctuations in the boundary-driven simulations are not quite so large as to mask the ordering of the two normal stress differences,

$$P_{xx} - P_{yy} > P_{xx} - P_{zz} .$$

Somewhat faster/larger computers could make this conclusion more convincing.

Table III. Soft-sphere viscosities in three dimensions with periodic boundary conditions. Space-and-time-averaged pressure tensors for homogeneous Sllod and Doll's algorithms using the soft-sphere pair potential illustrated in Fig. 6, $\phi = 100(1 - r^2)^4$. The energy and density are equal to unity and the strain rate, $\dot{\epsilon} = dv_x/dy$ is 0.50. The pressure-tensor components, are given in the order xx, yy, zz, xy with the kinetic, potential, and total terms indicated. The boundary conditions are periodic, with a total run time of 200x10,000 timesteps for $N = 10 \times 10 \times 10 = 1000$ with a fourth-order Runge-Kutta timestep of 0.005.

N	P_{xx}^K	P_{xx}^Φ	P_{xx}^Σ	P_{yy}^K	P_{yy}^Φ	P_{yy}^Σ	P_{zz}^K	P_{zz}^Φ	P_{zz}^Σ	P_{xy}^K	P_{xy}^Φ	P_{xy}^Σ
216S	0.506	2.012	2.518	0.497	2.014	2.511	0.493	1.991	2.483	-0.062	-0.282	-0.344
216D	0.496	2.004	2.499	0.507	2.022	2.529	0.493	1.991	2.484	-0.062	-0.281	-0.342
512S	0.506	2.010	2.516	0.497	2.012	2.509	0.493	1.989	2.483	-0.063	-0.280	-0.343
512D	0.496	2.001	2.496	0.507	2.021	2.528	0.493	1.990	2.483	-0.063	-0.281	-0.343
1000S	0.507	2.009	2.516	0.497	2.012	2.508	0.493	1.989	2.482	-0.063	-0.281	-0.344
1000D	0.496	2.000	2.496	0.507	2.021	2.528	0.493	1.989	2.482	-0.063	-0.280	-0.343
1728S	0.507	2.009	2.516	0.497	2.012	2.509	0.493	1.988	2.481	-0.063	-0.281	-0.344
1728D	0.496	2.001	2.497	0.508	2.020	2.528	0.493	1.989	2.481	-0.063	-0.281	-0.344
2744S	0.507	2.009	2.516	0.497	2.012	2.509	0.493	1.989	2.481	-0.063	-0.281	-0.344
2744D	0.496	2.000	2.496	0.508	2.020	2.528	0.493	1.989	2.482	-0.063	-0.280	-0.343

As the system size is increased, with the strainrate fixed, the Newtonian temperature increases also, in rough accord with the linear model treatment of Sec. II. That is, the central temperature increase is proportional to L^2 . Figure 12 shows temperature profiles for the three system sizes considered here. We consider the kinetic temperature here, because of its relative conceptual simplicity and its physical conceptual basis[37]. In the

Figure 10

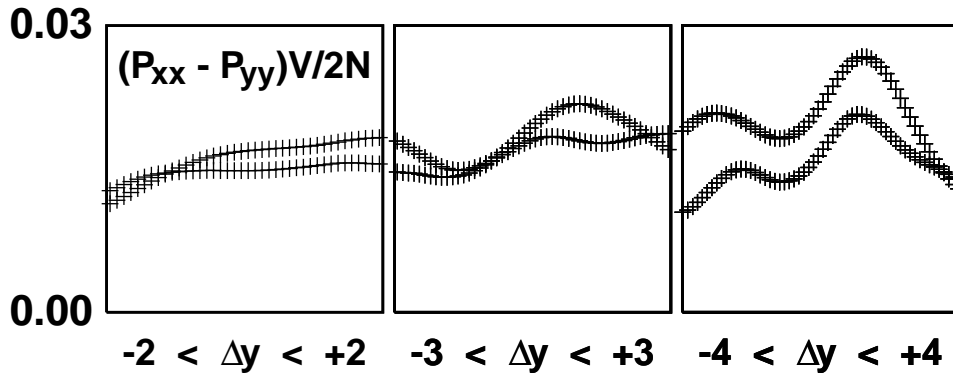


Figure 10: Normal stress differences for boundary-driven three-dimensional flows using the “soft-sphere” potential. The normal stress difference $(P_{xx} - P_{yy})V/2N$ is shown here for three different system sizes, with stress calculated relative to the *instantaneous* velocity profile. The spatially-averaged instantaneous particle values of velocity and stress are computed with w_{3D} . Then the particle values are averaged to get instantaneous profiles using w_{1D} . The figure shows time averages of those instantaneous profiles. Only data from the two distinct regions free of boundary averaging influences are shown here.

boundary-driven shear flows the *ordering* of the kinetic temperatures is

$$T_{xx} > T_{zz} > T_{yy} ,$$

with the difference between T_{xx} and T_{zz} two or three times larger than that between T_{zz} and T_{yy} .

IX. SUMMARY AND CONCLUSIONS

We were able to characterize the tensor temperature and the nonlinear stresses for both homogeneous and boundary-driven versions of simple shear. Neither Sllod nor Doll’s gives the correct ordering of the kinetic temperatures $\{ T_{ii} \}$. Generally the “Sllod” algorithm gives a somewhat “better” approximation to the normal-stress differences, $\{ P_{ii} - P_{jj} \}$, though Sllod is certainly far from “correct”. Despite its evident failures, there is a fairly widespread faith in the Sllod approach[60]. It is clear (as emphasized to us by Jim Lutsko; see also ref. [61]) that the algorithms’ extra rotational terms in the motion equations, $-\dot{\epsilon}p_x$ for Sllod and $-\dot{\epsilon}p_y$ for Doll’s, when left to their own devices, would eventually cause p_x^2 and T_{xx} to diverge for the Sllod algorithm, and p_y^2 and T_{yy} to diverge for Doll’s. This provides a clear explanation of the qualitative difference between the two algorithms’

Figure 11

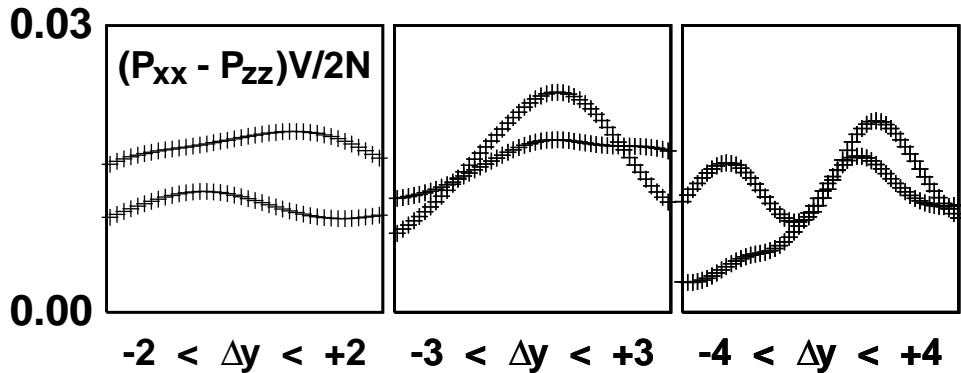


Figure 11: Normal stress differences for boundary-driven three-dimensional flows using the “soft-sphere” potential. The normal stress difference $(P_{xx} - P_{zz})V/2N$ is shown here for three different system sizes, with stress calculated relative to the *instantaneous* velocity profile. The spatially-averaged instantaneous particle values of velocity and stress are computed with w_{3D} . Then the particle values are averaged to get instantaneous profiles using w_{1D} . The figure shows time averages of those instantaneous profiles. Only data from the two distinct regions free of boundary averaging influences are shown here.

predictions and the corresponding opposite directions for the rotation of the principal axis of the stress.

Lutsko[62] has reviewed the hard-sphere-based Enskog theory for nonlinear stress (“the only viable theory”) and his finding that $P_{xx} > P_{yy}$ in simple shear is quite consistent with our results. On the other hand some theoretical models[63] and some computer simulations[16] find $P_{xx} < P_{yy}$, even for relatively simple fluids, so it is clear that more investigations are required. Evidently the temperature tensor and the nonlinear stresses are *not* given accurately by the Sllod algorithm. The more realistic boundary-driven flows need to be used whenever confidence in the results is required.

Boundary-driven flows are actually extremely complex, even for this simplest possible model of shear. The flows we can study are dominated by fluctuations which can be tamed by averaging, in one, two, or three dimensions, but the time-averaged flows describe the time-dependent situation no better than they would for a physical waterfall or a turbulent stream.

It is fortunate that a hydrodynamic description of flows *is* feasible on a very small scale (just a few particle diameters) as was apparent from the earliest shockwave simulations, which showed shockwidths of only a few particle diameters. It still remains a puzzle

Figure 12

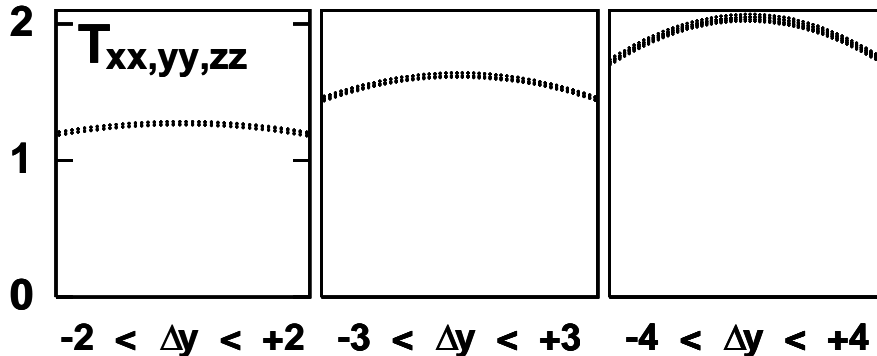


Figure 12: Tensor temperatures for boundary-driven three-dimensional flows using the “soft-sphere” potential. The time-averaged kinetic temperatures, relative to the instantaneous velocity profile, computed with w_{3D} and w_{1D} , are shown here for three system sizes, all with boundary temperatures and strain rates equal to 0.5. The systems contain four chambers with 10^3 (run length 1000), 12^3 (run length 500), and 14^3 (run length 400) particles per chamber in the three cases shown. Although data from the two distinct regions free of boundary averaging influences are shown here the differences between T_{xx} , T_{yy} , and T_{zz} , are of order ± 0.02 and are too small to see on the scale of the figure.

that shockwaves indicate an enhanced nonlinear viscosity while the homogeneous shear algorithms considered here predict a reduction rather than an enhancement[45].

X. ACKNOWLEDGMENTS

We thank Karl Travis and Billy Todd for providing some relevant literature and for stimulating our interest in the differences between the algorithms. Denis Evans kindly stated that there was no compelling reason to favor the Sllod algorithm for stationary flows. Debra Bernhardt made several useful comments on the manuscript. Jim Lutsko provided useful references and pointed out the physical reason underlying the positive nature of the normal stress difference $P_{xx} - P_{yy}$. The same explanation accounts also for the positive sign of $P_{xx} - P_{zz}$. See also the low-density Boltzmann equation treatment of shear flow[61]. We had considerable correspondence seeking evidence for logarithmic divergence of the two-dimensional shear viscosity, but found none. We specially thank Arek

Brańka[14], Giovanni Ciccotti[15], Michio Otsuke, and Hiroshi Watanabe for references, comments, and suggestions.

- [1] Wm. G. Hoover, *Computational Statistical Mechanics* (Elsevier, Amsterdam, 1991, available at the homepage <http://williamhoover.info/book.pdf>).
- [2] J. Petracic, *J. Chem. Phys.* **127**, 204702 (2007).
- [3] Wm. G. Hoover, *Smooth Particle Applied Mechanics — The State of the Art* (World Scientific Publishers, Singapore, 2006, available from the publisher at the publisher's site <http://www.worldscibooks.com/mathematics/6218.html>).
- [4] W. G. Hoover, *Lecture Notes in Physics* **132**, 373 (Springer-Verlag, Berlin, 1985).
- [5] D. J. Evans and G. P. Morriss, *Phys. Rev. A* **30**, 1528 (1984).
- [6] Wm. G. Hoover and W. T. Ashurst, *Theoretical Chemistry, Advances and Perspectives* **1**, 1 (Academic, New York, 1975).
- [7] W. T. Ashurst, Ph. D. thesis, University of California at Davis, 1974.
- [8] W. T. Ashurst and W. G. Hoover, *Phys. Rev. Lett.* **31**, 206 (1973).
- [9] S. Y. Liem, D. Brown and J. H. R. Clarke, *Phys. Rev. A*, **45**, 3706 (1992).
- [10] W. G. Hoover, W. T. Ashurst, and R. J. Olness, *J. Chem. Phys.* **60**, 4043 (1974).
- [11] T. Keyes and I. Oppenheim, *Phys. Rev. A* **8**, 937 (1973).
- [12] D. Gravina, G. P. F. Ciccotti, and B. L. Holian, *Phys. Rev. E* **52**, 6123 (1995).
- [13] B. Liu and J. Goree, *Phys. Rev. Lett.* **94**, 185002 (2005).
- [14] A. C. Brańka and D. M. Heyes, *Phys. Rev. E* **55**, 5713 (1997).
- [15] M. Ferrario, A. Fiorino, and G. P. F. Ciccotti, *Physica A* **240**, 268 (1997).
- [16] D. J. Evans and G. P. Morriss, *Statistical Mechanics of Nonequilibrium Liquids* (Academic, London, 1990, available at the authors' webpages).
- [17] J. L. Tuck and M. T. Menzel, *Adv. Math.* **9**, 399 (1972).
- [18] B. J. Alder and T. E. Wainwright, *J. Chem. Phys.* **31**, 459 (1959).
- [19] J. B. Gibson, A. N. Goland, M. Milgram, and G. H. Vineyard, *Phys. Rev.* **120**, 1229 (1960).
- [20] J. A. Barker and D. Henderson, *Annual Review of Physical Chemistry* **23**, 439 (1972).
- [21] J. F. Lutsko, *Phys. Rev. Lett.* **78**, 243 (1997).
- [22] Wm. G. Hoover, K. Boercker, and H. A. Posch, *Phys. Rev. E* **57**, 3911 (1998).

- [23] W. G. Hoover, D. J. Evans, R. B. Hickman, A. J. C. Ladd, W. T. Ashurst, and B. Moran, Phys. Rev. A **22**, 1690 (1980).
- [24] M. J. Gillan and M. Dixon, J. Phys. C **16**, 869 (1983).
- [25] D. J. Evans, Phys. Lett. A **91**, 457 (1982).
- [26] R. Zwanzig, Annual Review of Physical Chemistry **16**, 67 (1965).
- [27] K. Kadau, T. C. Germann, and P. S. Lomdahl, Int. J. Mod. Phys. C **17**, 1755 (2006).
- [28] M. Mareschal, J-P. Ryckaert, and A. Bellemans, Mol. Phys. **61**, 33 (1987).
- [29] P. J. Daivis, M. L. Matin, and B. D. Todd, J. Non-Newtonian Fluid Mech. **111**, 1 (2003).
- [30] B. D. Todd and P. J. Daivis, Phys. Rev. Lett. **81**, 1118 (1998).
- [31] A. Baranyai and P. T. Cummings, J. Chem. Phys. **110**, 42 (1999).
- [32] B. D. Todd and P. J. Daivis, Comp. Phys. Comm. **117**, 191 (1999).
- [33] D. M. Heyes, Chem. Phys. **98**, 15 (1985).
- [34] P. J. Daivis and B. D. Todd, J. Chem. Phys. **124**, 194103 (2006).
- [35] B. J. Edwards, C. Baig, and D. J. Keffer, J. Chem. Phys. **124**, 194104 (2006).
- [36] B. D. Todd and P. J. Daivis, Mol. Sim. **33**, 189 (2007).
- [37] Wm. G. Hoover and C. G. Hoover, Phys. Rev. E **77**, 041104 (2008).
- [38] D. J. Evans, E. G. D. Cohen, and G. P. Morriss, Phys. Rev. Lett. **71**, 2401 (1993).
- [39] D. J. Evans and D. J. Searles, Phys. Rev. E **50**, 1645 (1994).
- [40] G. Gallavotti and E. G. D. Cohen, Phys. Rev. Lett. **74**, 2694 (1995).
- [41] B. L. Holian, W. G. Hoover, and H. A. Posch, Phys. Rev. Lett. **59**, 10 (1987).
- [42] S. Nosé, J. Chem. Phys. **81**, 511 (1984).
- [43] W. G. Hoover, Phys. Rev. A **31**, 1695 (1985).
- [44] W. G. Hoover, A. J. C. Ladd, and B. Moran, Phys. Rev. Lett. **48**, 1818 (1982).
- [45] B. L. Holian, W. G. Hoover, B. Moran, and G. K. Straub, Phys. Rev. A **22**, 2798 (1980).
- [46] Wm. G. Hoover, Physica A **240**, 1 (1997).
- [47] C. P. Dettmann and G. P. Morriss, Phys. Rev. E **54**, 2495 (1996).
- [48] A. W. Lees and S. F. Edwards, J. Phys. C **5**, 1921 (1972).
- [49] W. Prager, *Introduction to the Mechanics of Continua* (Ginn & Company, Boston, 1961 [Dover reprint, 1973]).
- [50] Wm. G. Hoover and H. A. Posch, Phys. Rev. E **54**, 5142 (1996).
- [51] Wm. G. Hoover, K. Aoki, C. G. Hoover and S. V. De Groot, Physica D **187**, 253 (2004).

- [52] K. Aoki, and D. Kusnezov, *Phys. Lett. A* **265**, 250 (2000).
- [53] L. B. Lucy, *The Astronomical Journal* **82**, 1013 (1977).
- [54] Wm. G. Hoover, C. G. Hoover, and E. C. Merritt, *Phys. Rev. E* **69**, 016702 (2004).
- [55] O. Kum, Wm. G. Hoover, and H. A. Posch, *Phys. Rev. E* **52**, 4899 (1995).
- [56] H. A. Posch, Wm. G. Hoover, and O. Kum, *Phys. Rev. E* **52**, 1711 (1995).
- [57] Wm. G. Hoover and H. A. Posch, *Phys. Rev. E* **51**, 273 (1995).
- [58] P. J. Daivis, *J. Non-Newtonian Fluid Mech.* **152**, 120 (2008).
- [59] D. M. Gass, *J. Chem. Phys.* **54**, 1898 (1971).
- [60] Ch. Dellago and H. A. Posch, “Shear Viscosity and Lyapunov Instability of a Hard-Disk Couette Flow” (preprint, April 2008).
- [61] A. J. C. Ladd and W. G. Hoover, *J. Stat. Phys.* **38**, 973 (1985).
- [62] J. F. Lutsko, *Phys. Rev. E* **58**, 434 (1998).
- [63] H. H. Gan and B. C. Eu, *Phys. Rev. A* **46**, 6344 (1992).